CrossMark

# Backscattering and Line Broadening in Orion

C. R. O'Dell[1], G. J. Ferland[2], and J. E. Méndez-Delgado[3,4,5]
[1] Department of Physics and Astronomy, Vanderbilt University, Nashville, TN 37235-1807, USA
[2] Department of Physics and Astronomy, University of Kentucky, Lexington, KY 40506, USA
[3] Astronomisches Rechen-Institut, Zentrum für Astronomie der Universitat Heidelberg, Mönchhofstraße 12-14, D-69120 Heidelberg, Germany
[4] Instituto de Astrofísica de Canarias (IAC), E-38205 La Laguna, Spain
[5] Departamento de Astrofísica, Universidad de La Laguna, E-38206 La Laguna, Spain

## Abstract

Examination of emission lines in high-velocity-resolution optical spectra of the Orion Nebula confirms that the velocity component on the red wing of the main ionization front emission line is due to backscattering in the Photon Dominated Region. This scattered light component has a weak wavelength dependence that is consistent with either general interstellar medium particles or particles in the foreground of the Orion Nebula Cluster. An anomalous line-broadening component that has been known for 60+ years is characterized in unprecedented detail. Although this extra broadening may be due to turbulence along the line of sight of our spectra, we explore the possibility that it is due to Alfvén waves in conditions where the ratio of magnetic and thermal energies are about equal and constant throughout the ionized gas.

*Unified Astronomy Thesaurus concepts:* Emission nebulae (461); H II regions (694)

## 1. Introduction

The high surface brightness and proximity of the Orion Nebula (NGC 1976) has attracted hundreds of studies, from X-rays through long-wavelength radio rays. These studies have provided a basic model of the bright optical nebula (the Huygens Region), provided tests of basic photoionization theory as it applies to a density range of $10^4$, and revealed easily observed examples of the interaction of stellar winds and jets with nearby ambient material. Although the associated young stellar cluster is very rich, photoionization is dominated by two early spectral type stars, $\theta^1$ Ori C and $\theta^1$ Ori B, whose volumes of dominance are well identified. It is "everyone's nebula," and understanding it is a must for understanding other Galactic and extragalactic H II regions.

The current study furthers this goal by using the highest velocity resolution optical spectra from published studies and the public domain. These spectra are near the limit of what is possible, as their resolutions resolve the intrinsic line profiles of most of the optical emission lines. We find that there are processes operating (backscattered light and line broadening) that are usually not considered in the study of other nebulae. We explore these mechanisms in unprecedented detail by employing observations of a wide range of stages of ionization of the emitting gas.

## 2. Outline

In Section 3 we summarize earlier work that has led to this investigation, including discussion of the ionization structure of the Orion Nebula (Section 3.1), scattered starlight (Section 3.2), scattered emission lines (Section 3.3), and line widths (Section 3.4). Section 4 presents the database of spectra used and how they were analyzed. In the discussion Section 5 we analyze the velocities (Section 5.1), the properties of the

backscattered light forming the red shoulder on the line spectra profiles (Section 5.2), and the extra line broadening that is observed (Sections 6). Our conclusions are presented in Section 7.

## 3. Background of this Study

### 3.1. Ionization Structure

In this study, we ascribe the radiation from different observed ions as coming from layered emission zones. This is possible because it is well established that the bright Huygens Region is a concave ionized blister (Zuckerman 1973; Balick et al. 1974; Wen & O'Dell 1995) lying beyond the dominant ionizing star $\theta^1$ Ori C (O'Dell et al. 2017b).

The conditions of ionization are determined primarily by absorption of $\theta^1$ Ori C's radiation by the strong absorption edges of hydrogen (13.6 eV) and helium (24.6 eV; Osterbrock & Ferland 2006). Farthest from $\theta^1$ Ori C and the observer will be the hydrogen ionization boundary (IF) where $H^o \to H^+$, the limit where the hydrogen is either neutral or ionized. Closer still to $\theta^1$ Ori C will be a boundary where helium begins to be ionized. This means that there will be two ionization zones along a line of sight. The farthest is composed of $He^o + H^+$ and the closer is composed of $He^+ + H^+$. $\theta^1$ Ori C is too cool to produce an $He^{++}$ zone. Within the allowed zones, the stages of ionization of other atoms will be determined by their ionization energies. Oxygen becomes singly ionized by 13.6 eV and doubly ionized by 35.1 eV photons. This means that $O^+$ is found in the $He^o + H^+$ zone and $O^{++}$ in the $He^+ + H^+$ zone, giving rise to [O II] in the former and [O III] in the latter. Collectively, these zones will be called the Main Ionization Front (MIF), thus distinguishing it from scattered light or emission from any foreground layers (O'Dell 2018).

This ionization stratification determines the region of emission of the various ions observed in this study. [O I] arises from exactly at the hydrogen ionization boundary (the IF), while [S II] arises in a region near that boundary but within the $He^o + H^+$ zone (a layer we will designate as the "Near IF Zone" or "Near-IF"). Within the $He^o + H^+$ zone (designated

here as the "Low Ionization Zone" or "Low-IZ") will also be found [O II], [N II], [Cl II], and [Fe III] emission. In the $He^{+}+H^{+}$ zone (designated as the "High Ionization Zone" or "High-IZ") we will find emission from the He I recombination lines and the [Ne III], [O III], [S III], and [Ar III] forbidden lines. Of course hydrogen recombination lines arise both in the $He^{o}+H^{+}$ and the $He^{+}+H^{+}$ zones (the "Hydrogen Emitting Zone" or "H-Z"). Dynamic modeling of the nebula (Henney 2003) leads to the expectation that emission closest to the ionization boundary will be close to that of the underlying Photon Dominated Region ($27.5 \pm 1.5$ km s$^{-1}$,[6] Goicoechea et al. 2015) and the host Orion Molecular Cloud (OMC) $25.9 \pm 1.5$ km s$^{-1}$ (O'Dell 2018), while emission from successively higher ionization will be progressively more blueshifted. In the remainder of the paper we give the results for the helium singlet lines (He lines) separately and also within the High-IZ, where the lines originate. This treatment of the hydrogen and helium lines permits the comparison of their recombination line characteristics with the other lines that arise from collisional excitation.

We give below a list of the acronyms used in the text. The corresponding regions of emission are ordered with increasing distance along a ray passing from the host molecular cloud toward the dominant ionizing star.

OMC: the host Orion Molecular Cloud
PDR: the Photon Dominated Region
IF: the ionization front where $H^{o} \rightarrow H^{+}$
Near-IF: the portion of the $He^{o}+H^{+}$ zone near the IF
Low-IZ: the $He^{o}+H^{+}$ zone
High-IZ: the $He^{+}+H^{+}$ zone
H-Z: the hydrogen emitting combined $He^{o}+H^{+}$ and $He^{+}+H^{+}$ zones
MIF: all of the ionized zones
$\theta^{1}$ Ori C: the dominant ionizing star

### 3.2. Scattered Starlight

Beyond the IF lies a dust-rich dense layer of atoms and molecules constituting a Photon Dominated Region (PDR; Tielens & Hollenbach 1985; Tielens et al. 1993). The dust component can backscatter any optical radiation impinging on it. Greenstein & Henyey (1939) first noted that the nebular continuum is much stronger than expected for an ionized gas and attributed this to scattering of $\theta^{1}$ Ori C radiation by dust within the nebula. The excess continuum in several H II regions, including the Orion Nebula, was reported on in Shajn et al. (1955) where it was concluded that the Orion Nebula's extra continuum was due to scattered starlight. This interpretation was refined as the presence of the PDR was recognized, and now we believe that the excess continuum is due to backscattering. More recent studies have quantitatively measured the amount of the excess and the overall flux distribution of the nebular radiation (O'Dell & Hubbard 1965; O'Dell & Harris 2010).

### 3.3. Scattered MIF Emission Lines

The earliest high spectral resolution studies of the Huygens Region (Castañeda 1988; Jones 1992; O'Dell & Wen 1992)

showed a consistent pattern of a red shoulder on emission-line profiles. The most probable interpretation was identified in O'Dell et al. (1992). Backscattering by grains in the PDR of emission lines from the MIF are to be expected, based on the well-established scattering of $\theta^{1}$ Ori C's radiation. Because the emitting layers are blueshifted with respect to the PDR's velocity, the backscattered velocity component will appear as a redshifted shoulder (at velocity $V_{scat}$) on the MIF's emission at a velocity displacement of about twice the velocity difference of the emitting and scattering layers (the photoevaporation velocity). This interpretation was confirmed in a modeling study of scattered light by Henney (1994), who demonstrated that the double shift was a good upper limit for the scattered light velocity.

This means that the velocity difference of the MIF component ($V_{mif}$) and that of the PDR ($V_{PDR}$) is a useful measure of the component's photoevaporation velocity and the difference of velocity $V_{scat} - V_{mif}$ becomes a useful diagnostic of the physical structure of the nebula, especially in the sub-Trapezium region where the MIF is nearly in the plane of the sky (Wen & O'Dell 1995). This tool has been used in numerous studies by the lead author of this paper and his collaborators (O'Dell 2001, 2018; Abel et al. 2016, 2019; O'Dell et al. 2017a, 2017b, 2020a, 2020b). The ability to accurately measure the backscattered component will primarily depend on the velocity difference ($V_{scat} - V_{mif}$), the signal ($F_{scat}$) relative to that of the MIF ($F_{mif}$), that is, $F_{scat}/F_{mif}$, and the intrinsic line width (usually expressed as the FWHM signal). This means that low-mass ions like hydrogen and helium are intrinsically broad through thermal broadening and their $V_{scat}$ components are correspondingly difficult to measure. By contrast, higher-mass ions such those producing [S II] will be easier to measure. However, in the case of [O I] and [S II] the velocity shift $V_{scat} - V_{mif}$ is expected to be small, thus compensating for the narrower line widths, rendering $V_{scat}$ difficult to measure in these ions.

The question of detection is discussed in detail in O'Dell (2018), using an [N II] line, where detection of a blueshifted component is tested. Multiple measurements of red components and using the probable errors generated by the profile fitting program (task "splot" of IRAF[7]) shows that the threshold of detectability is $F_{scat}/F_{mif} \cong 0.03$. Ratios below this level were not used in the current study. This turned out to only apply to $F_{scat}/F_{mif}$ in the [O I] and [S II] lines.

Our study determines the $F_{scat}/F_{mif}$ ratio for an unprecedented number of emission lines, covering a unique number of ionization states. One of our goals has been to use this ratio to study the structure of the MIF emission and to possibly determine the wavelength dependence of the backscattering.

### 3.4. Line Broadening

At the same time that the early high spectral resolution spectra revealed the presence of a red shoulder due to backscattering, it was also noted that the line widths were of unexpected width. This was first noted earlier in a high-resolution optical photographic study by Wilson et al. (1959), where the extra width was assigned to turbulence (Münch 1958). If this component is due to mass motion, it carries as much energy as the thermal motion of the gas.

---

[6]    All velocities in this paper are heliocentric. They may be converted to the LSR system preferred by radio and infrared astronomers by subtracting 18.2 km s$^{-1}$.

[7]    IRAF is distributed by the National Optical Astronomy Observatories, which is operated by the Association of Universities for Research in Astronomy, Inc., under cooperative agreement with the National Science Foundation.
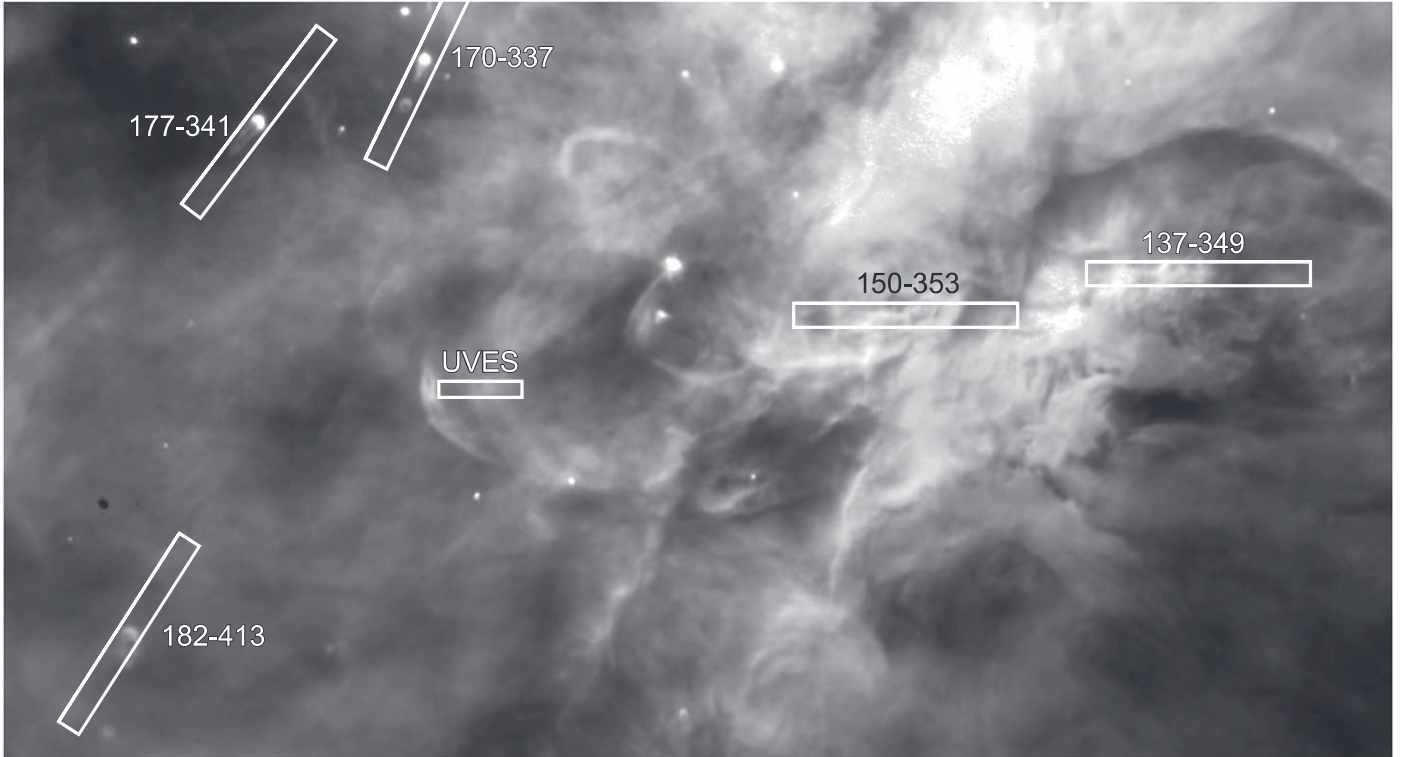
**Figure 1.** This Hubble Space Telescope F656N WFPC image is $86\rlap{.}{''}8 \times 47\rlap{.}{''}2$ and centered on 5:35:15.82–5:23:57.0 (2000). It shows the location of the samples used in this study (Section 4).

Although known for over one-half century, this component has defied a clear interpretation. The most complete discussion of the Extra Line Broadening Component (ELBC) and its interpretation appears in O'Dell et al. (2017b). Our study extends that investigation, using a wider variety of emission lines.

The observed FWHM ($W_{obs}$) will be the quadratic addition of the thermal broadening, the resolution of the spectrograph being used ($R$), and any fine-structure component ($W_{fs}$). Anticipating that this study will reveal an additional line-broadening component, called in O'Dell et al. (2017b) the ELBC, this component must be included. Using the characteristic electron temperature of 9200 K (Méndez-Delgado et al. 2021), the expected observed $W_{obs}$ in km s$^{-1}$ will be

$$W_{obs} = [438.1/A + \text{ELBC}^2 + R^2 + W_{fs}^2]^{\frac{1}{2}} \qquad (1)$$

where $A$ is the atomic mass of the emitting ion. The $438.1/A$ term arises from thermal broadening and is proportional to the electron temperature. If one ignores the ELBC component, the temperature dependence of the relation allows one to derive an electron temperature by observing the FWHM of two lines of very different masses. This has typically been done using H$\alpha$ or H$\beta$ lines together with the strong [O III] or [N II] lines. Because the ELBC component can be important, the derived temperatures are incorrect. Méndez-Delgado et al. (2021) tried to improve this method of temperature determination using assumptions about the nature of the ELBC, following a procedure introduced in García-Díaz et al. (2008).

Even in those lines where $F_{scat}/F_{mif}$ cannot be determined, $W_{obs}$ can be accurately derived, thus allowing the determination of the ELBC. One of the main contributions of the present study is the measurement of many lines originating from multiple ionization zones, which allows for an unprecedented study of the line broadening.

## 4. Analysis of Existing Spectra

We have drawn on two sets of existing slit spectra.

The first source is from the study of Méndez-Delgado et al. (2021), which was an echelle slit investigation of the high-ionization shocks that compose HH 529. Since we were interested in the nebula's radiation, we selected a $5\rlap{.}{''}2$ long and $1\rlap{.}{''}0$ wide sample at 5:35:16.73–5:23:57$\rlap{.}{''}6$ free (except at large blueshifts) of shock emission. This spectrum was made with the UVES spectrograph of the Very Large Telescope. The position of our sample is shown in Figure 1, where it is labeled UVES. The HH 529 shocks lie well removed in velocity from the layers producing the ambient emission-line spectra of this region and are created in the High-IZ cavity near $\theta^1$ Ori C (Blagrave et al. 2007). Aside from these foreground shocks, the MIF in this region is quiescent, as shown in Figure 15 of García-Díaz et al. (2008).

The second source was Keck I Telescope High Resolution Echelle Spectrometer (HIRES) spectra made with $14''$ slits centered on proplyds and other regions of particular interest. Portions of the slits were sampled avoiding the proplyds or when the large blueshift emission could be avoided. They are described in Henney & O'Dell (1999). Each of these subsamples were observed several times, so that there are typically about twenty spectra for each pointing. The full length entrance slits are shown in Figure 1 and are labeled with the targeted object's position in the system introduced in O'Dell & Wen (1992).
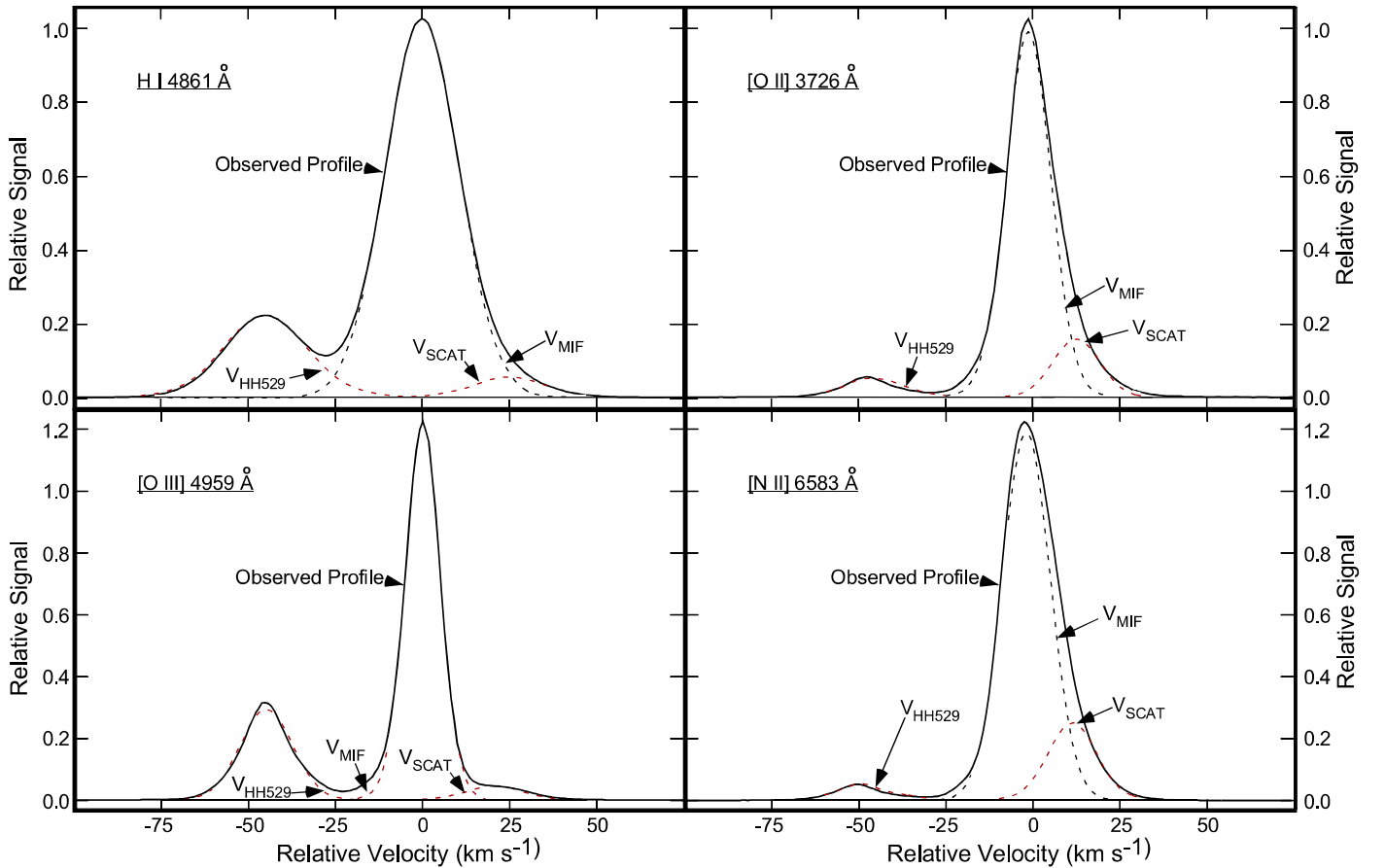
**Figure 2.** This figure shows the observed profiles for four UVES lines. The upper panel is for the H$\beta$ line and the lower is for the [O III] 4959 Å line. The velocity scale is relative to $V_{\text{mif}}$ for that line as given in Table 1. Solid lines show the observed line profiles, while the dashed red lines give the three component fits obtained with IRAF task "splot." The blueshifted component labeled HH 529 is from one of that object's shocks. They are relatively weaker for lower-ionization MIF lines. They are not important in analysis of the $V_{\text{scat}}$ components because their backscattered components would be at about 70 km s$^{-1}$.

The spectra were resolved into multiple velocity components using the IRAF package of data processing tools, especially the task "splot," as was done in multiple previous studies. Often only an assumption of two components (MIF the strongest and the much weaker backscattered component). In some cases a well-separated blue component arising from the jets and shocks was also fit. The task "splot" yields the signal, velocity, and FWHM for each component and its probable errors. An illustration of an "splot" analysis of a narrow and a broad emission line is shown in Figure 2. Comparison of the H I 4861 Å and [O III] 4959 Å lines shows the advantages in measuring the $V_{\text{scat}}$ component in lines with a small thermal broadening component. Even though the velocity separation of $V_{\text{mif}}$ and $V_{\text{scat}}$ is smaller for the [O II] 3726 Å doublet lines and the [N II] 6583 Å line, the right-hand panels show that their $F_{\text{scat}}/F_{\text{mif}}$ ratios are large and measurable. The significance of this result is discussed in detail in Section 5.2.

For the UVES samples, the derived values appear in Table 1. In that table ions appear grouped into the ionization zones described in Section 3.1 and are ordered with increasing wavelength for each ion. Each column ordered left to right presents: the ionization zone and ion, the assumed at rest wavelength of the emission line, $V_{\text{mif}}$, $V_{\text{scat}} - V_{\text{mif}}$, $F_{\text{scat}}/F_{\text{mif}}$, and the derived ELBC using the observed FWHM, an assumed electron temperature of 9200 K (Méndez-Delgado et al. 2021), fine-structure broadening components from García-Díaz et al. (2008), and a resolution of $R = 7.5$ km s$^{-1}$.

The probable errors are those given by "splot." It should be noted that no He I triplet lines appear because they have strong fine-structure broadening, something absent in the singlets.

The same results are given given in Table 2 for the HIRES observations. The results are ordered in terms of decreasing $V_{\text{mif}}$. There were about 20 samples measured for each line and we show uncertainties determined by the spread of values within each line. Derivation of the ELBC component was the same as for the UVES spectra, but now a resolution of $R = 6.2$ km s$^{-1}$ was adopted.

In Table 1 we have placed the results for [Cl II] in the Near-IF because the transition from Cl$^0$ to Cl$^+$ occurs at 13.0 eV and from Cl$^+$ to Cl$^{++}$ at 23.8 eV. This means that some or most of the [Cl II] emission occurs at or near the IF, where the velocity will be that of the IF or Near-IF. Like the [S II] emission lines, no $V_{\text{scat}}$ component was detected.

## 5. Discussion

In this section we discuss what can be learned from the $V_{\text{mif}}$ values, the $F_{\text{scat}}/F_{\text{mif}}$ ratio, and the ELBC values.

### 5.1. Velocities

Because the velocity of the PDR must vary across the Huygens Region, as the local tilt of the PDR changes (O'Dell 2018), we limit our interpretation of the velocities to

**Table 1**
Data for All UVES Sample Lines[a,b]

| Ion | $\lambda_o$ (Å) | $V_{mif}$ | $V_{scat} - V_{mif}$ | $F_{scat}/F_{mif}$ | ELBC |
|---|---|---|---|---|---|
| IF | ... | ... | ... | ... | ... |
| [O I] | 6300.304 | 28.1 ± 0.0 | ... | ... | 7.9 ± 0.2 |
| [O I] | 6363.776 | 28.1 ± 0.1 | ... | ... | 8.1 ± 0.0 |
| Near-IF | ... | ... | ... | ... | ... |
| [S II] | 4068.600 | 22.3 ± 0.0 | ... | ... | 16.2 ± 0.2 |
| [S II] | 6716.440 | 23.4 ± 0.0 | ... | ... | 19.5 ± 0.1 |
| [S II] | 6730.820 | 23.4 ± 0.0 | ... | ... | 18.5 ± 0.1 |
| [S II] | 10320.490 | 21.2 ± 0.0 | ... | ... | 19.6 ± 0.5 |
| [S II] | 10336.410 | 21.4 ± 0.0 | ... | ... | 19.9 ± 0.6 |
| [Cl II] | 9123.600 | 24.1 ± 0.2 | ... | ... | 18.7 ± 0.7 |
| Low-IZ | | | | | |
| [O II] | 3726.030 | 18.3 ± 0.0 | 13.4 ± 0.0 | 0.18 ± 0.01 | 7.4 ± 0.1 |
| [O II] | 3728.820 | 15.1 ± 0.0 | 14.1 ± 0.0 | 0.17 ± 0.00 | 12.6 ± 0.0 |
| [N II] | 6548.050 | 20.7 ± 0.0 | 13.4 ± 0.0 | 0.17 ± 0.00 | 13.6 ± 0.1 |
| [N II] | 6583.450 | 18.4 ± 0.0 | 12.9 ± 0.0 | 0.21 ± 0.00 | 13.2 ± 0.1 |
| [Fe III][c] | 4658.10 | 17.9 ± 0.4 | 12.8 ± 0.1 | 0.19 ± 0.00 | 8.6 ± 0.1 |
| [Fe III][c] | 4881.11 | 12.7 ± 0.5 | 12.3 ± 0.5 | 0.20 ± 0.01 | 8.9 ± 0.3 |
| High-IZ | ... | ... | ... | ... | ... |
| [Ne III] | 3868.75 | 15.8 ± 0.0 | 17.0 ± 0.0 | 0.08 ± 0.00 | 7.2 ± 0.1 |
| [Ne III] | 3967.46 | 15.5 ± 0.0 | 22.1 ± 0.3 | 0.06 ± 0.00 | 7.9 ± 0.1 |
| [O III] | 4363.21 | 14.7 ± 0.0 | 23.1 ± 0.9 | 0.06 ± 0.00 | 9.1 ± 0.1 |
| [O III] | 4958.910 | 16.4 ± 0.0 | 21.6 ± 0.1 | 0.05 ± 0.00 | 7.2 ± 0.1 |
| [O III] | 5006.840 | 17.4 ± 0.0 | 23.1 ± 0.1 | 0.06 ± 0.00 | 6.7 ± 0.1 |
| [S III] | 6312.070 | 16.3 ± 0.0 | 17.9 ± 0.1 | 0.11 ± 0.00 | 10.3 ± 0.2 |
| [S III] | 9530.980 | 15.8 ± 0.0 | 21.2 ± 0.11 | 0.10 ± 0.00 | 9.9 ± 0.1 |
| [Ar III] | 7135.790 | 15.2 ± 0.0 | 16.7 ± 0.0 | 0.09 ± 0.00 | 6.3 ± 0.1 |
| [Ar III] | 7751.100 | 16.1 ± 0.0 | 18.6 ± 0.1 | 0.08 ± 0.01 | 6.5 ± 0.2 |
| He lines | ... | ... | ... | ... | ... |
| He | 3964.730 | 15.8 ± 0.0 | 22.1 ± 1.6 | 0.05 ± 0.01 | 9.5 ± 0.2 |
| He | 4921.930 | 15.8 ± 0.0 | 19.6 ± 0.5 | 0.10 ± 0.00 | 7.8 ± 0.1 |
| He | 5015.680 | 16.3 ± 0.0 | 19.0 ± 0.5 | 0.10 ± 0.00 | 6.7 ± 0.2 |
| He | 6678.150 | 16.0 ± 0.0 | 20.0 ± 0.2 | 0.06 ± 0.00 | 7.5 ± 0.3 |
| He | 7281.350 | 16.5 ± 0.0 | 19.4 ± 0.0 | 0.10 ± 0.00 | 7.3 ± 0.0 |
| H-Z | ... | ... | ... | ... | ... |
| H9 | 3835.4 | 14.3 ± 0.0 | 25.9 ± 0.8 | 0.05 ± 0.00 | 11.6 ± 0.2 |
| H7 | 3970.08 | 15.4 ± 0.0 | 26.8 ± 0.2 | 0.04 ± 0.00 | 11.0 ± 0.1 |
| H6 | 4101.71 | 17.4 ± 0.0 | 27.5 ± 0.1 | 0.08 ± 0.00 | 11.5 ± 0.1 |
| H$\gamma$ | 4340.47 | 15.0 ± 0.0 | 24.2 ± 0.1 | 0.05 ± 0.00 | 10.2 ± 0.1[d] |
| H$\beta$ | 4861.35 | 15.8 ± 0.0 | 23.6 ± 0.1 | 0.06 ± 0.00 | 9.8 ± 0.1[d] |
| H$\alpha$ | 6562.79 | 16.0 ± 0.0 | 25.2 ± 0.1 | 0.05 ± 0.00 | 11.0 ± 0.1[d] |
| Pa12 | 8750.46 | 16.7 ± 0.0 | 23.6 ± 0.0 | 0.07 ± 0.00 | 9.4 ± 0.1 |
| Pa11 | 8862.89 | 12.6 ± 0.0 | 23.0 ± 0.1 | 0.09 ± 0.00 | 9.2 ± 0.0 |

**Notes.**
[a] All velocities are in km s$^{-1}$ and heliocentric for $V_{mif}$.
[b] rms indicates the root-mean-squared deviation of a value, as determined from the IRAF task "splot."
[c] Not included in the average for the Low-IZ $V_{mif}$ values, as explained in Section 5.1.
[d] Includes correction of line width for fine-structure broadening, using values from García-Díaz et al. (2008).

the single sample in the UVES observations. These are summarized in Table 3. For reference, the average $V_{PDR}$ for the Huygens Region as determined from [C II] 158 $\mu$m is 27.5 ± 1.5 km s$^{-1}$ (Goicoechea et al. 2015) and is indistinguishable the same in the region of the UVES observations. CO emission must occur slightly further into the host cloud, and in Table 3.3.VII of Goudis (1982) the average velocity is 27.3 ± 0.3 km s$^{-1}$. We have grouped the results by their ionization zones, as explained in Section 3.1. This is more meaningful than presenting them by the ion's ionization energies, as frequently done. Ionization energies are what determine the region of emission, which in turn then determines the velocity, rather than the ionization energies directly determining the velocity.

Because the ionized gas nearest to the IF is of higher density than gas further away, first-order considerations lead to the expectation that the higher-ionization lines will have more negative velocities. This was the assumption that led Zuckerman (1973) and Balick et al. (1974) to establish that the Huygens Region was a more distant thin emitting layer, rather than a basically symmetric distribution of clumped gas around $\theta^1$ Ori C. This expectation was confirmed in detailed modeling by Henney et al. (2005).

This sense of variation in $V_{mif}$ agrees with the values in Table 3. The two [Fe III] $V_{mif}$ values are very different, 17.9 ± 0.4 km s$^{-1}$ for the stronger 4658 Å line and 12.7 ± 0.5 km s$^{-1}$ for the 4881 Å line. These lines both result from collisional excitations out of the 3d$^6$ $^5$D$_4$ ground state of Fe$^{++}$.

**Table 2**
Averaged Data from Keck I HIRES Observations[a,b]

| Line | $V_{\rm mif}$ | $V_{\rm scat} - V_{\rm mif}$ | $F_{\rm scat}/F_{\rm mif}$ | ELBC |
|---|---|---|---|---|
| [O I] 6300 Å | $27.7 \pm 1.8$[c] | ... | ... | $10.3 \pm 1.8$ |
| [S II] 6731 Å | $23.7 \pm 1.9$ | $15.5 \pm 3.2$ | $0.08 \pm 0.04$ | $13.6 \pm 2.5$ |
| [N II] 6583 Å | $20.9 \pm 1.8$ | $14.4 \pm 1.8$ | $0.09 \pm 0.04$ | $11.1 \pm 1.6$ |
| [O III] 5007 Å | $20.7 \pm 1.9$ | $14.0 \pm 4.5$ | $0.06 \pm 0.04$ | $11.2 \pm 2.7$ |
| [O III] 4959 Å | $17.7 \pm 2.0$ | $15.8 \pm 4.3$ | $0.06 \pm 0.03$ | $10.8 \pm 2.5$ |
| Hα 6563 Å | $17.2 \pm 3.5$ | $23.2 \pm 3.9$ | $0.11 \pm 0.06$ | ...[d] |
| Hβ 4861 Å | $15.3 \pm 3.5$ | $24.1 \pm 3.8$ | $0.09 \pm 0.07$ | ...[d] |

**Notes.**
[a] Averaged over five slits and about 20 samples for each line.
[b] All velocities are in km s$^{-1}$ and heliocentric for $V_{\rm mif}$.
[c] All rms errors are determined from the scatter of about twenty samples for each line.
[d] ELGC not calculated because most of the line width is due to thermal broadening.

**Table 3**
Averaged Data for UVES Zones[a]

| Group | $V_{\rm mif}$ | $V_{\rm scat} - V_{\rm mif}$ | $F_{\rm scat}/F_{\rm mif}$ | ELBC |
|---|---|---|---|---|
| IF ([O I]) | $28.1 \pm 0.1$ | ... | ... | $8.0 \pm 0.1$ |
| Near-IF ([S II]+[Cl II]) | $22.6 \pm 1.2$ | ... | ... | $18.7 \pm 1.3$ |
| Low-IZ | $18.1 \pm 2.3$ | $13.2 \pm 0.6$ | $0.19 \pm 0.02$ | $11.9 \pm 3.9$ |
| High-IZ | $15.9 \pm 0.8$ | $20.1 \pm 2.6$ | $0.08 \pm 0.02$ | $7.9 \pm 1.5$ |
| He lines | $16.1 \pm 0.3$ | $20.0 \pm 1.2$ | $0.08 \pm 0.02$ | $8.2 \pm 1.9$ |
| High-IZ+He lines | $16.0 \pm 0.6$ | $20.1 \pm 2.1$ | $0.08 \pm 0.02$ | $8.0 \pm 1.6$ |
| H-Z | $15.4 \pm 1.5$ | $25.0 \pm 1.6$ | $0.06 \pm 0.02$ | $10.5 \pm 0.9$ |

**Note.**
[a] All velocities are in km s$^{-1}$ and heliocentric for $V_{\rm mif}$.

The difference is probably due to uncertainties in their intrinsic wavelengths. This is recognized in Méndez-Delgado et al. (2021), and the upper right panel of their Figure 13 shows that the $V_{\rm mif}$ for this ion is about 17 km s$^{-1}$, consistent with the Low-IZ average of $18.1 \pm 2.3$ km s$^{-1}$. The uncertainty in intrinsic wavelength of each line does not affect their $V_{\rm scat} - V_{\rm mif}$ values, and we have used them in deriving that average.

In Table 3 we see a steady blueshift progression of $V_{\rm mif}$ values from IF through the High-IZ, as predicted by the Henney et al. (2005) study. The He lines value of $16.1 \pm 0.3$ km s$^{-1}$ lies within the value of $15.9 \pm 0.8$ km s$^{-1}$ for the High-IZ, as it should be according to the arguments presented in Section 3.1. The only expected difference would be due to the fact that the collisionally excited forbidden lines used in calculating the average for High-IZ would selectively come from high-temperature gas along the line of sight, while the recombination He I lines would come from any lower-temperature gas.

Hydrogen recombination lines will arise from all of the ionization zones, their total emission being redder close to the high-density IF and bluer from any low electron temperature components. At $V_{\rm mif} = 15.4 \pm 1.5$ km s$^{-1}$, its value is indistinguishable from the High-IZ+He lines value of $16.0 \pm 0.6$ km s$^{-1}$.

As noted in Section 3.3, the expectation is for $V_{\rm scat} - V_{\rm mif}$ to be approximately twice the evaporation velocity of the emitting gas. That evaporation velocity will be $V_{\rm PDR} - V_{\rm mif}$. We adopt

$V_{\rm PDR} = 27.5 \pm 1.5$ km s$^{-1}$ (from [C II]) and calculate expected $V_{\rm scat} - V_{\rm mif}$ values of IF 0 km s$^{-1}$, Near-IF $10 \pm 2$ km s$^{-1}$, Low-IZ $15 \pm 2$ km s$^{-1}$, and High-IZ $23 \pm 3$ km s$^{-1}$. The observed values of $13.2 \pm 0.6$ and $20.1 \pm 2.6$ km s$^{-1}$ for the two outer zones are in good agreement with the assumption that the $V_{\rm scat}$ components are due to backscattering. A $V_{\rm scat}$ component is not seen for [O I], which is not surprising because any backscattering component would be buried under the $V_{\rm mif}$ component. We do not see a $V_{\rm scat}$ component for [S II] in the UVES spectra. However, there is one at $V_{\rm scat} - V_{\rm mif} = 15.5 \pm 3.2$ km s$^{-1}$ for the higher signal-to-noise ratio HIRES sample, which is in marginal agreement with the expected value of $10 \pm 2$ km s$^{-1}$, although there is a caveat to be stated above that the HIRES samples may include different tilts of the IF. However, this caveat may not apply, since $V_{\rm mif}$ for [O I] is very similar for HIRES ($27.7 \pm 1.8$) and UVES ($28.1 \pm 0.1$).

In a fundamental paper on the expansion of a photoionized blister of gas, Henney et al. (2005) explained the blueshifts of lines arising from the MIF of the Huygens Region. The predictions of their model for a slightly concave PDR agree well with the velocity gradients seen in the strongest emission lines and in the various stages of ionization we study in this paper.

The above conclusions are essentially the same as in earlier studies (O'Dell et al. 2020a) that examined only [N II] and [O III] spectra from a number of locations. What this study has done is to expand the list of emission lines, increasing the accuracy of testing and confirming the photoevaporation model of the MIF and backscattering from the PDR.

### 5.2. Characteristics of the $F_{scat}/F_{mif}$ Ratio

The $F_{\rm scat}$ component of a spectrum is formed by backscattering in the optically thick PDR. This means that the $F_{\rm scat}/F_{\rm mif}$ ratio is determined by the albedo and backscattering phase function of the dust particles in the PDR, and possibly the distance between the emitting and scattering layers. Previous studies of the red shoulder of [N II] and [O III] emission lines found a wide range of $F_{\rm scat}/F_{\rm mif}$ values with a range of near zero to about 0.2. One of the goals of this study was to characterize this ratio over a wide range of wavelengths and ionization states.

In Figure 3, we present the results for the UVES and HIRES spectra, where it is important to recall that the UVES values are from a single sample and the HIRES values are the average of about twenty spectra within five samples. We detected a $V_{\rm scat}$ component in all of our zones except IF and Near-IF. There, the $V_{\rm mif}$ values are so close to $V_{\rm PDR}$ that any expected backscattering would be hidden under the red shoulder of the $V_{\rm mif}$ profile. The data are coded by symbols (filled boxes for UVES, filled circles for HIRES) and by colors for the emission zone. The error bars for the HIRES data are much larger, which probably reflects the variety of conditions in the multiple samples in five areas; however, their average values are similar to multiwavelength values for the UVES sample.

The striking outlying values all arise from the UVES Low-IZ. Within this set the much weaker [Fe III] lines agree with the [N II] and [O II] lines. It is possible that the small velocity separation of the $V_{\rm mif}$ and $V_{\rm scat}$ components prohibits accurate measurement of the $V_{\rm scat}$ component in the red shoulder of the $V_{\rm mif}$ component. However, the strength of the $V_{\rm scat}$ components shown in Figure 2 and the small uncertainties of the derived

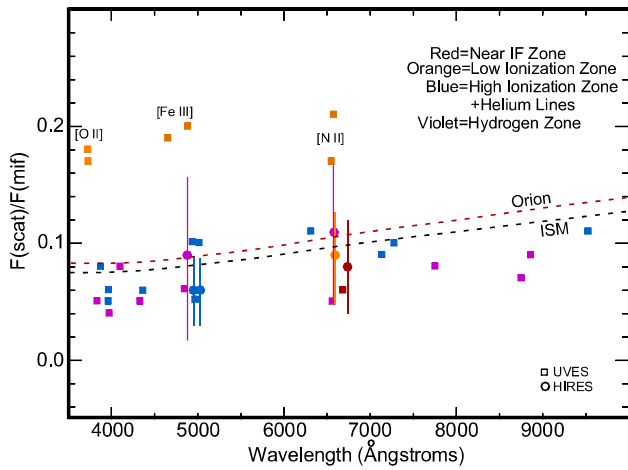**Figure 3.** The ratio of backscattered light to the source of that line's emission ($F_{scat}/F_{mif}$) is shown as a function of wavelength. Determination for the UVES (Méndez-Delgado et al. 2021) sample are depicted with small boxes and the HIRES samples (Henney & O'Dell 1999) as filled circles. Error bars for the HIRES values were determined from the scatter of values from typically 20 separate spectra. The UVES error bars were determined using the IRAF task "splot." When no error bar is shown, it is no greater than the size of the symbol. The dashed lines indicate the expected relation for backscattering from an optically thick PDR (Section 5.2.1).

deconvolution argue that the ratios are accurate. It may be that the small separation of the Low-IZ and the PDR is the cause, although to first order this should not be a factor in emission and scattering from two plane parallel layers. Certainly, the Low-IZ zone is much closer to the PDR than the High-IZ+He lines and the H-Z. The layer emitting [N II] has a characteristic thickness of 0.003 pc (corresponding to $1''$ in the plane of the sky), and the [O III] characteristic thickness is about 0.06 pc (corresponding to $20''$), as derived in O'Dell (2001). In addition, the Low-IZ zone is highly structured, as shown by the much greater detail seen in images made in the low-ionization states, whereas the higher-ionization layers are smoother.

We can only conclude that the much higher values of $F_{scat}/F_{mif}$ are likely to be real, even though the reasons are not established.

### 5.2.1. A Possible Wavelength Dependence of the Backscattering

Any wavelength dependence of the $F_{scat}/F_{mif}$ ratio may be a useful diagnostic of the nature of the particles in the PDR. The line-of-sight reddening to field stars is determined by a combination of absorption and diffuse scattering of interstellar particles, with a well-established result that the extinction curve in the outer layers of the Orion Nebula are flatter than in the general interstellar medium. The easiest and most common interpretation is that foreground Orion particles are larger than those usually encountered (Baldwin et al. 1991). In the case of our observations the $F_{scat}/F_{mif}$ ratio becomes a measure of backscattering by particles.

In Figure 3, one sees that for the Near-IF and the other zones there are systematic patterns. For the Near-IF points, the value of $F_{scat}/F_{mif}$ is essentially constant, with a hint of a drop at the 3727 Å [O II] doublet. For emission lines from the other zones, we see that $F_{scat}/F_{mif}$ is again nearly flat, with a believable indication of a drop in the ratio at the shortest wavelengths.

### 5.2.2. Expected Wavelength Dependence

Studies of scattered starlight have been concentrated on the Merope reflection nebula in the Pleiades star cluster (O'Dell 1965; Gibson & Nordsieck 2003), where it was found that the scattered continuum was much redder than the illuminating star. However, this object is optically thin in visual wavelengths and the scattering layer is in the foreground of the star (Gibson & Nordsieck 2003). This invalidates any comparison with Orion because dust in Orion's PDR must be optically thick and the scattering layer lies beyond the source of the emission.

Henney (1998) initially modeled scattering of light in Orion's PDR, extending those calculations in Appendix B of a later paper (Ferland et al. 2012). There, it was established that the principal dependency was the single-scattering albedo and the scattering asymmetry. In W. J. Henney (2022, private communication), it was reported that calculating the expected wavelength dependence for particles typical of the general interstellar medium (reddening ratio $R_V = 3$) and the foreground material reddening the starlight and nebular emission ($R_V = 5$). With Henney's permission we have added these predictions to Figure 3. There is a remarkable general agreement of his predictions with the observations (except for the Low-IZ Zone, where those ratios are anomalous; Section 5.2).

## 6. The Extra Line-broadening Component

### 6.1. Earlier Discussions of the ELBC

There have been multiple earlier studies with modern CCD detectors that have characterized the FWHM in various emission lines and over a range of spectrograph resolutions. Some results come from studies pursuing interpretation of fine-scale velocities of the MIF in hopes of explaining these as evidence of turbulent motion (Castañeda 1988; Jones 1992; O'Dell & Wen 1992; Wen & O'Dell 1993).

These results have been summarized in an earlier discussion of the ELBC (O'Dell et al. 2017a), but a reevaluation is presented here because we now limit our HIRES data to the inner parts of the Huygens Region and have $W_{obs}$ values for many additional ions and lines. We gather in Table 4 the data obtained in the same region as our UVES and HIRES samples. This table also presents the results from the current study and a weighted average of ELBC from all the studies for each line. We do not use the $W_{obs}$ values for several lines from García-Díaz et al. (2008) because they adopt a fundamentally different method of analyzing the line profiles.

### 6.2. Derivation of the ELBC

As noted in Section 3.4, the observed line width (as measured by its FWHM) depends on several factors: the atomic mass ($A$), the electron temperature, any fine-structure component ($W_{fs}$), and the velocity resolution of the spectrograph employed ($R$). The earliest high-resolution optical studies of the strongest emission lines indicated that these factors failed to explain the observed FWHM ($W_{obs}$), which led to the introduction of an additional broadening term (the ELBC). Equation (1) can then be rewritten to isolate the ELBC component as

$$\text{ELBC} = [W_{obs}^2 - 438.1/A - R^2 - W_{fs}^2]]^{\frac{1}{2}} \quad (2)$$

**Table 4**
Summary of ELBC Values Including Earlier Studies

| Line | Earlier Source | Spectrograph | Resolution | ELBC (Earlier[a]) | ELBC (UVES[b]) | ELBC (HIRES[c]) | ELBC (ave[d]) |
|---|---|---|---|---|---|---|---|
| [O I], 6300 Å | O'Dell & Wen (1992) | FEED | 4.7 km s$^{-1}$ | 8.9 (1) | 7.9 ± 0.2(4) | 10.3 ± 1.8(3) | 8.9 ± 1.2 |
| [S II], 6731 Å | ⋯ | ⋯ | ⋯ | ⋯ | 18.8 ± 0.1(4) | 13.6 ± 2.5(2) | 17.1 ± 2.7 |
| [N II], 6583 Å | ⋯ | ⋯ | ⋯ | ⋯ | 13.2 ± 0.1(4) | 11.1 ± 1.6(2) | 12.5 ± 1.1 |
| [O II], 3729 Å | Jones (1992) | FEED | 4.7 km s$^{-1}$ | 10.5 ± 2.5(2) | 12.6 ± 0.0(4) | ⋯ | 11.9 ± 1.1 |
| [S III], 6312 Å | Wen & O'Dell (1993) | FEED | 4.7 km s$^{-1}$ | 11.0(1) | 10.3 ± 0.2(4) | ⋯ | 10.4 ± 0.3 |
| [O III], 5007 Å | Castañeda (1988) | FEED | 4.0 km s$^{-1}$ | 8.6 ± 0.1(4) | 6.7 ± 0.1(4) | 11.2 ± 2.7(2) | 8.4 ± 1.7 |

**Notes.**
[a] The Coudé Feed Spectrograph at the KPNO observatory (Castañeda 1988).
[b] The UVES spectrograph at the Very Large Telescope.
[c] The HIRES spectrograph on the Keck I 10 m telescope.
[d] Weights are given in parentheses.

where an electron temperature of 9200 K (Méndez-Delgado et al. 2021) is assumed. We adopted the fine-structure line-broadening constants of García-Díaz et al. (2008) for Hα, Hβ, and Hγ. We show the derived ELBC values in Table 2 for the HIRES spectra, Table 4 for various previous high-resolution optical studies, and Table 3 for the UVES zones. We also show the derived ELBC values from the various emission-line studies and an H64α study (Wilson et al. 1997; O'Dell et al. 2003) in Figure 4.

### 6.3. Derived ELBC Values

We have used the procedure described in the preceding section to derive ELBC values from the $W_{obs}$ determination for all the samples under consideration. Although most fall into a value near 9 km s$^{-1}$, there are some anomalies that require a different interpretation.

#### 6.3.1. ELBC in the Hydrogen Lines

The most difficult ion for extracting ELBC is hydrogen ($A = 1$) because of its large thermal broadening and the presence of a fine-structure component. The large thermal component means that the derived ELBC is sensitive to the electron temperature. Therefore the clearest values of ELBC for hydrogen lines is for the UVES data where the same data set was used for deriving the electron temperature, so any uncertainty of the thermal component should be small.

The average value of ELBC for the UVES hydrogen lines ($10.5 ± 0.9$ km s$^{-1}$) falls near the values derived from other ions (about 9 km s$^{-1}$).

#### 6.3.2. Other Ions

At helium ($A = 4$), we have only the results from UVES. Their ELBC values are grouped around $7.8 ± 1.1$ km s$^{-1}$. The helium results are expected to be accurate, as the thermal broadening component is smaller and the He I lines arise only from the High-IZ.

The oxygen values cluster within 1 km s$^{-1}$ around 9.5 km s$^{-1}$. Oxygen is present in all of the ionization zones ([O I] at the IF, [O II] in the Low-IZ, and [O III] in the High-IZ).

The results for ELBC from [Ne III] ($A = 20$), [Ar III] ($A = 40$), and [Fe III] ($A = 56$) all lie near the values for UVES (H I), He I, and oxygen. The [N II] ($A = 14$) values from both HIRES and UVES lie slightly higher than this grouping.
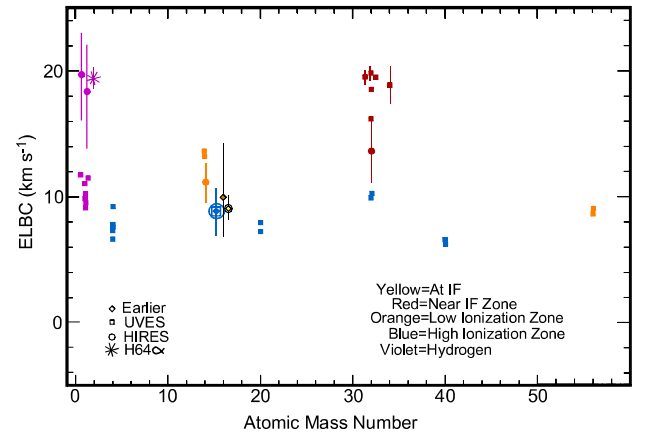


**Figure 4.** The unexplained ELBC values determined by quadratic extraction from the observed $W_{obs}$ as explained in Section 6 are presented. In order to identify any dependence of ELBC on the zone giving rise to the line, the data have been color coded, with the symbols having the same meaning as in Figure 3. Entries for oxygen from the same ionization zone were averaged. Where the oxygen results were crowded, the plotted $A$ values were shifted by 0.5. The error bars were determined as in Figure 3. The data point for hydrogen at $19.6 ± 0.9$ km s$^{-1}$ is from a study of H64α by Wilson et al. (1997), with the ELBC value calculated in O'Dell et al. (2003).

Because the line (6583 Å) is well resolved from the nearby Hα line (6563 Å), contamination should not be a problem.

Although ELBCs for the [S III] lines (6313 and 9531 Å) lie near the values from most of the other ions and lines, there is an unexpected wide range for the [S II] lines. These are discussed in Section 6.3.3.

#### 6.3.3. Anomalous Values of H I, [S II], and [Cl II] Lines

The ELBC results for H I in the radio H64α (Wilson et al. 1997) and HIRES samples are quite different from those in the UVES sample. The UVES region is quiescent and unaffected by the high-ionization shocks in HH 529 that lie well into the foreground, whereas the HIRES samples are all from those with proplyds or high-velocity features.

One thing that is different from the other observations is the spatial resolution. Wilson et al. (1997) employed a beamwidth of 42″ and the HIRES slit samples were about 7″ long, while our UVES sample was 5″.2 long. Since the HIRES and UVES samples are of similar sizes, the explanation probably does not lie with the spatial resolution but in the nature of the region in our UVES sample.

The HIRES and H64$\alpha$ values would come into agreement with the UVES data if the electron temperature was about 13,000 K, which is much higher than theoretically expected. This is because at a higher temperature the thermal component correction of the broadening would be larger and for a fixed $W_{obs}$, the derived ELBC would be reduced. Although the hydrogen emission comes from throughout the ionized gas, because it is seen in recombination, the emissivity is weighted toward lower temperatures. Therefore it is unlikely that the large ELBC values are due to higher electron temperatures.

The HIRES result for 6731 Å ($13.6 \pm 2.5$ km s$^{-1}$) could be explained by higher electron temperatures in those samples. However, this cannot be invoked for explaining the high UVES 6731 Å values because the temperature there is accurately determined. The same can be said for the [Cl II] ion ($18.7 \pm 0.7$ km s$^{-1}$), as determined from the 9124 Å line. The fact that both [S II] and [Cl II] emission arise from the Near-IF argues for a common explanation. This could be much higher turbulence in this transition zone, or more intense magnetic fields where the condition of a frozen-in field is established.

W. J. Henney (2022, private communication) has pointed out that the UVES sample lies in a quiescent region, as noted in Section 4. By contrast, all of the HIRES samples lie in regions that systematically show higher values of the ELBC (see Figure 16 of García-Díaz et al. 2008). This could account for the high value of ELBC found from the HIRES H$\alpha$ data and the H64$\alpha$ results at a resolution of 42″. This could be also be true for the somewhat high values in the HIRES [N II] and [S II] data. However, this cannot explain the anomalously high values from the UVES [S II] and [Cl II]. The variation between sample regions emphasizes that the UVES values are to be employed for an explanation of the ELBC.

## 6.4. Explanation of the ELBC

The problems that confront us are to explain the cause of the ELBC that we find in most samples (the band of values at about 9 km s$^{-1}$ across Figure 4) and the high values of ELBC that are seen in H I in the HIRES samples, in the H65$\alpha$ sample, and in the [S II] and [Cl II] UVES samples.

### 6.4.1. Earlier Attempts to Explain the ELBC

Henney et al. (2005) investigated the role that the velocity gradient in a photoevaporation flow has in broadening an emission line and producing the ELBC. They conclude that photoevaporation contributes little to the line broadening and then evaluated the role that might be played by Alfvén waves. They concluded that these waves could explain their value for ELBC in [S III] (9 km s$^{-1}$) if the magnetic field was approximately $10^{-3}$ G, but concluded that in general Alfvén waves do not provide a natural explanation for the line broadening.

The ELBC was also explored in detail in Section 6.1.2 of O'Dell et al. (2017a), where they evaluated the role of the expansion velocity of [N II], considering both quadratic and linear addition. They too concluded that evaporation flow was not a major contributor to the ELBC. Their data set used HIRES results and the García-Díaz et al. (2008) atlas spectra, exploring grouping of ELBC according to ionization zones and forbidden versus recombination lines. The homogeneity and multiplicity of lines in the current study render that discussion moot, except for the qualitative argument that the answer could

be due to photoevaporative flow off of dense knots in the PDR as modeled by Mellema et al. (2006), although this was not considered quantitatively in any detail.

### 6.4.2. The ELBC May Be Explained by Alfvén Waves

Magnetic fields in H II regions and the associated PDRs have previously been established, a good review appearing in Ferland (2009). Jess et al. (2009) successfully explained the nonthermal line widths in the lower layers of the Sun's atmosphere as being due to Alfvén waves, and Roshi (2007) determined in 14 samples of H II regions that Alfvén waves explained the nonthermal components of singly ionized carbon radio recombination lines.

It is well established that there are strong magnetic fields in the Huygens Region. In their examination of absorption lines in the closer (to $\theta^1$ Ori C) Veil component (called layer B), Troland et al. (1989, 2016) found values for the line-of-sight magnetic field of about 50 $\mu$G, far above the usual values for the interstellar medium. In an analysis of the energy parameters, they found that most of the energy was in the magnetic field. This is similar to the conclusion of Abel et al. (2016) that layer B in the Veil is in rough equipartition.

The presence of a strong magnetic field in the PDR, which is much closer to the MIF than the Veil, has been derived from observations of polarization in far-infrared thermal emission from aligned dust grains Chuss et al. (2019). Their "H II region" sample, which is close to our UVES sample, found a plane-of-the-sky value of $0.29 \pm 0.03$ mG. This value is probably too low, as they assumed that the thermal grain emission comes from a layer 0.14 pc thick. Goicoechea et al. (2016) show in their Atacama Large Millimeter/submillimeter Array study of HCO$^+$ in the highly tilted Bright Bar that the apparent thickness of the PDR is 30″, which corresponds to a distance of 0.06 pc at an adopted distance of 388 pc (Kounkel et al. 2016). Under the assumption that the PDR thickness is the same in both the Bright Bar and their "H II region" sample, the true derived magnetic field in the plane of the sky is twice as large as their value, and the 3D field will be even larger.

Henney et al. (2005) give the formula for Alfvén wave velocities $V_A^2 = B^2/4\pi\rho$, where $\rho$ is the mass density of the gas. Assuming that the gas is fully ionized and dominated by the mass of hydrogen, this equation becomes $V_A^2$ (km s$^{-1}$) $= 4.79 \times 10^{12} B^2/n_e$, where $n_e$ is the electron density. For $n_e \sim 10^4$ electrons cm$^{-3}$, this becomes $V_A^2$ (kms$^{-1}$) $= 4.79 \times 10^8 B^2$. If $B = 1$ mG, then $V_A \cong 21.9$ km s$^{-1}$. This is in approximate agreement with ELBC $= 9$ km s$^{-1}$, similar to the conclusion of Henney et al. (2005) for their [S III] line. However, this approximate agreement does not make it clear that it can explain the constancy of ELBC across the ionization zones since we have no a priori knowledge of the variations in $B$ with ionization.

Troland et al. (2016) present equations for the total thermal and magnetic field energy densities as $E_{therm} = (3/2) nkT$ and $E_{mag} = B^2/8\pi$. The ratio of the magnetic and thermal energy densities ($\beta$) in a fully ionized volume will then be $\beta = B^2/(12\pi kTn_e)$. Substituting the ratio $B^2/n_e$ into the $V_A$ equation gives $V_A^2 = 3kT\beta/m_H$. Inserting numerical values for the constants and assuming that the electron temperature is $10^4$ K, then expressing the velocity in the convenient units of km s$^{-1}$ gives $V_A^2 = 249 \times \beta$. Since the ELBC component is 9 km s$^{-1}$, this argues that $\beta = 0.33$, and the magnetic and thermal energies are about equal. If the ELBC is caused by Alfvén

waves, and ELBC is nearly constant in all the ionization zones, this argues that $\beta$ is about equal throughout. This means that the ratio $B^2/n_e$ is constant as $n_e$ drops with increasing distance from the PDR. How the observed strong magnetic field in the PDR is coupled to the inferred magnetic field in the outflowing ionized gas and the inferred $B^2/n_e$ constancy is not addressed here.

In the models of Orion created by Henney et al. (2005), the effects of magnetic fields in an expanding photoionized layer were considered and in some regions were quite important. A much more elaborate set of H II region models, now giving full consideration of magnetic fields, is described in Arthur et al. (2011). Although the latter study employed the most complete considerations of the MHD processes invoked by the presence of a magnetic field, none of those models simulates the Huygens Region specifically. A magnetic-field-free statistical analysis of ELBC and radial velocities by Arthur et al. (2016) demonstrated that the observed ELBC was about 1.5 times larger than expected from the point-to-point velocity variations, but that this could be explained by turbulence in the ionized regions. Since turbulence must be present, then the derived Alfvén wave velocities are upper limits.

We consider the explanation of the ELBC to be an open subject. Alfvén waves are attractive because of the simplicity of a constant near energy equilibrium of the thermal gas and the magnetic field. Its relation to the strong field in the PDR may be due to its being frozen in with the plasma. In this case the magnetic field lies are trapped into the expanding ionized gas. The exact nature of Alfvén waves in conditions within the interstellar medium remains a long-standing problem in the discipline.

### 6.4.3. Explanation of the Anomalously High ELBC Values

In Section 6.3.3, we present the arguments for the extraordinarily large ELBC values for the HIRES and H64$\alpha$ being due to those samples coming from regions of larger ELBC values, whereas the lower values for the UVES sample are because that region is genuinely more quiescent. Within a model invoking the importance of Alfvén waves, the extraordinarily large UVES ELBC values for [S II] and [Cl III] could be due to dominance by the magnetic field in the narrow region of ionized gas closest to the PDR.

## 7. Conclusions

1. The observed velocity gradient agrees with the expectation of viewing a nearly flat-on, photoevaporating ionization front.
2. The separation of the $V_{\mathrm{mif}}$ and $V_{\mathrm{scat}}$ is consistent with the red shoulder of the emission lines being due to backscattering in the PDR.
3. The backscattering component is stronger when the emitting layer is close to the PDR, being about half as strong when the emitting layer is further away in the He$^+$+H$^+$ zone.
4. There is a suggestion of a wavelength dependence of the strength of the backscattered light, it being somewhat lower at shorter wavelengths.
5. The slight wavelength dependence of the backscattering is consistent with models adopting characteristics of either the interstellar medium or the Orion cluster.

6. An extra component contributing to the emission-line widths is certainly present, generally being about 9 km s$^{-1}$.
7. Although this extra line broadening of emission lines can be attributed to turbulence, it can also be explained by Alfvén waves in a medium where the ratio of magnetic energy and thermal energy is constant.
8. Anomalously high line broadening is encountered in the Near-IF zone in the UVES sample and in the HIRES hydrogen and radio H64$\alpha$ samples; the former are probably due to dominance by the magnetic field, and the latter due to the HIRES and H64$\alpha$ sampling more turbulent regions.

### Data Availability

The UVES data were from observations collected at the European Southern Observatory, Chile, proposal no. ESO 092C-0323(A), on the nights of 2013 November 28 and 29 using the Very Large Telescope in Cerro Paranal, Chile, and are available in their archives. The data are described in Appendix D2 of Méndez-Delgado et al. (2021), and their processing is described in Section 2 of the same publication. The Keck HIRES observations and processing are described in Henney & O'Dell (1999), and were obtained on the nights of 1997 December 5 and 6 and are available through the Keck Observatory Archives.

### ORCID iDs

C. R. O'Dell ⓘ https://orcid.org/0000-0003-3323-2310
G. J. Ferland ⓘ https://orcid.org/0000-0003-4503-6333
J. E. Méndez-Delgado ⓘ https://orcid.org/0000-0002-6972-6411

## References

Abel, N. P., Ferland, G. J., & O'Dell, C. R. 2019, ApJ, 881, 130
Abel, N. P., Ferland, G. J., O'Dell, C. R., & Troland, T. H. 2016, ApJ, 819, 136
Arthur, S. J., Henney, W. J., Mellema, G., De Colle, F., & Vázquez-Semadeni 2011, MNRAS, 414, 1747
Arthur, S. J., Medina, S.-N. X., & Henney, W. J. 2016, MNRAS, 423, 2864
Baldwin, J. A., Ferland, G. J., Martin, P. G., et al. 1991, ApJ, 374, 580
Balick, B., Gammon, R. H., & Hjellming, R. M. 1974, PASP, 86, 616
Blagrave, K. P. M., Martin, P. G., Rubin, R. H., et al. 2007, ApJ, 655, 299
Castañeda, H. O. 1988, ApJS, 67, 93
Chuss, D. T., Andersson, B. G., Bally, J., et al. 2019, ApJ, 872, 187

Ferland, G. J. 2009, in Proc. IAU Symp. 259, Cosmic Magnetic Fields: From Planets, to Stars and Galaxies (Cambridge: Cambridge Univ. Press), 25

Ferland, G. J., Henney, W. J., O'Dell, C. R., Porter, R. L., & Williams, R. J. R. 2012, ApJ, 757, 79

García-Díaz, Ma.-T., Henney, W. J., López, J. A., & Doi, T. 2008, RMxAA, 44, 181

Gibson, S. J., & Nordsieck, K. H. 2003, ApJ, 589, 362

Goicoechea, J. R., Pety, J., Cuadrado, S., et al. 2016, Natur, 537, 207

Goicoechea, J. R., Teyssier, D., Etxaluze, M., et al. 2015, ApJ, 812, 75

Goudis, C. 1982, The Orion Complex: A Case Study of Interstellar Matter (Dordrecht: Reidel), doi:10.1007/978-94-009-7712-9

Greenstein, J. L., & Henyey, L. G. 1939, ApJ, 89, 647

Henney, W. J. 1994, RMxAA, 29, 192

Henney, W. J. 1998, ApJ, 503, 760

Henney, W. J. 2003, RMxAA, 15, 175

Henney, W. J., Arthur, S. J., & García-Díaz, M.-T. 2005, ApJ, 627, 813

Henney, W. J., & O'Dell, C. R. 1999, AJ, 118, 2350

Jess, D. B., Mathioudakis, M., Erdélyi, R., et al. 2009, Sci, 323, 1582

Jones, M. R. 1992, PhD thesis, Rice Univ.

Kounkel, M., Hartmann, L., Loinard, L., et al. 2016, ApJ, 834, 142

Mellema, G., Arthur, S. J., Henney, W. J., Iliev, I., & Shapiro, P. 2006, ApJ, 647, 397

Méndez-Delgado, J. E., Esteban, C., García-Rojas, J., et al. 2021, MNRAS, 502, 1703

Münch, G. 1958, RvMP, 30, 1035

O'Dell, C. R. 1965b, ApJ, 142, 604

O'Dell, C. R. 2001, ARA&A, 39, 9

O'Dell, C. R. 2018, MNRAS, 478, 1017

O'Dell, C. R., Abel, N. P., & Ferland, G. J. 2020a, ApJ, 891, 46

O'Dell, C. R., Abel, N. P., & Ferland, G. J. 2020b, ApJ, 907, 119

O'Dell, C. R., Ferland, G. J., & Peimbert, M. 2017a, MNRAS, 464, 4835

O'Dell, C. R., & Harris, J. A. 2010, AJ, 140, 985

O'Dell, C. R., & Hubbard, W. B. 1965, ApJ, 142, 591

O'Dell, C. R., Kollatschny, W., & Ferland, G. J. 2017b, ApJ, 837, 151

O'Dell, C. R., Peimbert, M., & Peimbert, A. 2003, AJ, 125, 2590

O'Dell, C. R., Walter, D. K., & Dufour, R. J. 1992, ApJL, 399, L67

O'Dell, C. R., & Wen, Z. 1992, ApJ, 387, 229

Osterbrock, D. E., & Ferland, G. J. 2006, Astrophysics of Gaseous Nebulae and Active Galactic Nuclei (2nd ed.; Mill Valley, CA: Univ. Science Books)

Roshi, D. A. 2007, ApJL, 658, L41

Shajn, G. A., Hase, V. T., & Pikelner, S. B. 1955, Liege Institute of Astronomy Conferences, 6, 441

Tielens, A. G. G. M., & Hollenbach, D. 1985, ApJ, 291, 747

Tielens, A. G. G. M., Meixner, M. M., van der Werf, P. P., et al. 1993, Sci, 262, 86

Troland, T. H., Goss, W. M., Brogan, C. L., Crutcher, R. M., & Roberts, D. A. 2016, ApJ, 825, 2

Troland, T. H., Heiles, C., & Goss, W. M. 1989, ApJ, 337, 342

Wen, Z., & O'Dell, C. R. 1993, ApJ, 409, 262

Wen, Z., & O'Dell, C. R. 1995, ApJ, 438, 784

Wilson, O. C., Münch, G., Flather, E. M., & Coffeen, M. A. 1959, ApJS, 4, 199

Wilson, T. L., Filges, L., Codella, C., Reich, W., & Reich, P. 1997, A&A, 327, 1177

Zuckerman, B. 1973, ApJ, 183, 163